

Optimising a model of ultrasonic waves propagating in a buffer rod

by

G.D. Henstra

to obtain the degree of Bachelor of Science
at the Delft University of Technology,
to be defended publicly on Wednesday December 20th, 2017 at 10:00.

Student number: 4307690
Project duration: September 11, 2017 – December 20, 2017
Thesis committee: MSc. S. Mastromarino TU Delft, supervisor
Dr. ir. M. Rohde, TU Delft
Dr. ir. D. Lathouwers, TU Delft

An electronic version of this thesis is available at <http://repository.tudelft.nl/>.

logo_black.pdf

Abstract

New nuclear power plants can be part of the solution to global warming and the increasing energy demand worldwide. The Molten Salt Fast Reactor (MSFR) has great advantages regarding safety, economic competitiveness, resistance against proliferation and also sustainability. For the design of the MSFR, the thermodynamic properties of the fuel must be accurately measured. Since conventional measurement techniques can not be used due to the corrosiveness, the high temperature and the radioactivity of the molten salt, a new measurement setup using ultrasound is being developed. In the setup, the use of a suitable waveguide is indispensable to isolate the ultrasonic transducer from the adverse conditions of the molten salt. When the ultrasonic waves propagate through the waveguide and the fluid, the density and the viscosity of the fluid can be determined by measuring the reflection coefficient and the attenuation of the wave. The pulse-echo response to be measured is deteriorated by trailing echoes. For this research, a buffer rod is used as waveguide and this research aims at optimising the simulation in COMSOL of waves propagating through the buffer rod. In order to accurately model the buffer rod, the mesh and time discretisation was optimised first. Repetitive simulations showed that at least 8 element per wavelength are needed for meshing the model. For determining the time-step used in the solver, a Courant number of 1/10 gave accurate results while maintaining a reasonable computation time. Using this discretisation, the optimal tapering angle to reduce trailing echoes was found for multiple buffer rods. It was concluded that a wide buffer rod results in less trailing echoes than a narrow buffer rod. Another technique to reduce trailing echoes is using irregular shaped polygonal buffer rods with an odd number of sides. 3D models have been made to verify this idea but due to a lack of computational power, the simulations could not be run.

$$R = \frac{Z_2 - Z_1}{Z_2 + Z_1} \quad (1)$$

Contents

1	Introduction	1
1.1	The Molten Salt Fast Reactor	1
1.1.1	Advantages to solid fuel reactors	1
1.1.2	SAMOFAR	2
1.2	Properties of the molten salt	3
1.3	Ultrasonic wave method	3
1.4	Aim of this research	5
2	Theory of acoustic waves	6
2.1	Bulk waves in fluids	7
2.1.1	Acoustic wave equations	7
2.1.2	Attenuation in a fluid	7
2.2	Bulk waves in solids	8
2.2.1	Stress and strain tensor	8
2.2.2	Elastic wave equations	9
2.2.3	Longitudinal wave speed	9
2.2.4	Shear wave speed	10
2.3	Wave characteristics at boundaries	10
2.3.1	Solid-liquid interface	11
2.3.2	Solid-Air Interface	12
2.4	Calculations of thermodynamic properties	12
2.4.1	Density calculation	12
2.5	Explanation measurement plot	14
2.6	Trailing echoes	15
2.6.1	Wave propagation simulation in COMSOL Multiphysics	15
2.6.2	Head waves	15
2.6.3	Conversion from shear waves to longitudinal wavefront	16
2.6.4	Radiated edge waves	16
2.7	Reducing trailing echoes	17
2.7.1	Buffer rod tapering	17
2.7.2	Polygonal buffer rods	18
3	Simulation model	20
3.1	General properties in COMSOL	20
3.1.1	Wave packet	20
3.1.2	Boundary conditions	20
3.1.3	Dimensions and size	21

3.1.4	Study type	21
3.1.5	Materials	21
3.1.6	Measuring in COMSOL	21
3.2	Discretisation of simulation model	22
3.2.1	Literature review on meshing	22
3.2.2	Meshing in the simulations	22
3.2.3	Literature review on time-stepping	22
3.2.4	Time stepping in the simulations	23
4	Results and discussion	24
4.1	Mesh density	24
4.2	Time stepping	24
4.3	Verification of the model	26
4.3.1	Copper	26
4.3.2	Titanium	27
4.4	Tapering angle simulations	29
4.5	Reducing computation cost for 3D models	30
4.6	Comparison 2D and 3D models	31
4.7	Polygonal buffer rods	32
5	Conclusion	33
5.1	Recommendation	33
	Appendices	35
A	Measurements for changing tapering angle	36
B	Matlab code for wave speed determination	37

Chapter 1

Introduction

Nuclear power plants, which produce low CO₂ emission electricity [21] at competitive costs, can be part of the solution to global warming and the increasing energy demand worldwide. In order to guarantee the future role of nuclear energy and improve the public perception, constant improvement of nuclear technology is needed. The energy transition might be one of the most interesting subjects of the 21st century and nuclear energy has great potential to become a key player in this problem. The common perception of nuclear power however is not entirely positive due to the catastrophic accidents of Three Mile Island (1979), Chernobyl (1986) and Fukushima (2011).

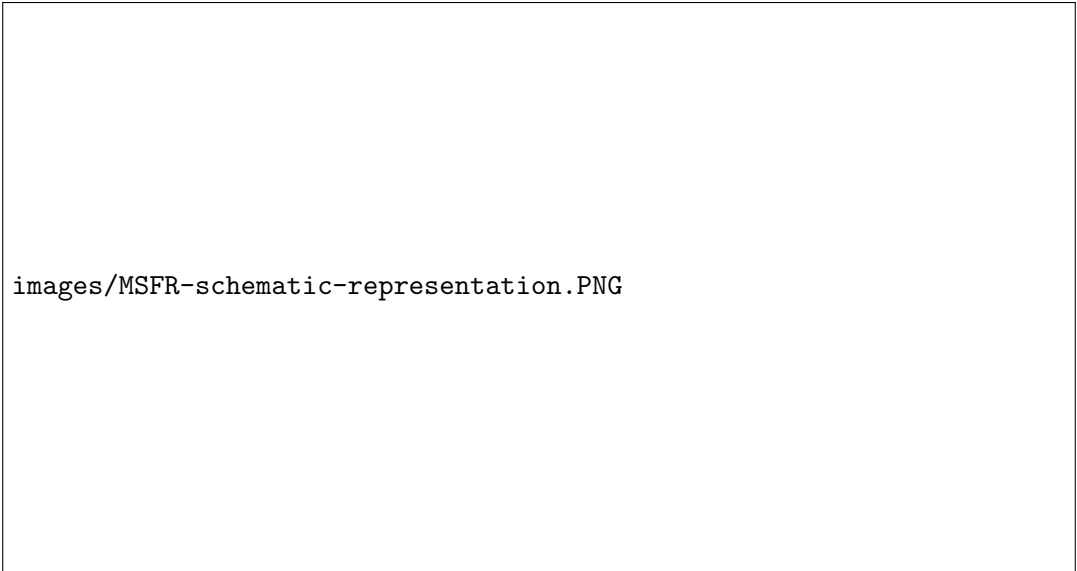
In 2000, during the Generation IV International Forum, an international collective representing governments of 14 countries was initiated. The countries participating were countries where nuclear energy is important now and vital for the future. In two years, about one hundred of the concepts for new nuclear reactors were reviewed [2]. In late 2002, the selection of six reactor technologies, which the collective's participants believed represented the future shape of nuclear energy, was announced. The Generation IV Nuclear Reactors were selected on the basis of being clean, safe and cost-effective means of meeting increased energy demands on a sustainable basis, while being resistant to a diversion of materials for weapons proliferation and secure from terrorist attacks. These reactors are: Very-High-Temperature Reactor (VHTR), Molten Salt Reactor (MSR), Supercritical-Water-Cooled Reactor (SCWR), Gas-Cooled Fast Reactor (GFR), Sodium-cooled fast reactor (SFR) and the Lead-cooled fast reactor (LFR). A variant of one of the designs, the Molten Salt Fast Reactor (see figure 1.1), is investigated by an European project named SAMOFAR.

1.1 The Molten Salt Fast Reactor

1.1.1 Advantages to solid fuel reactors

Nowadays, most of the nuclear reactors are pressurised water reactors, in which a solid fuel generates energy due to fission of atoms. This heat is absorbed by the primary coolant (water) that transfers its thermal energy to steam, which spins an electric generator.

One of the six proposed designs of the Generation IV reactor is the Molten Salt Fast Reactor (MSFR). Whereas nearly all nuclear reactors use a solid fuel, the Molten Salt Fast Reactors is characteristic of the use of a liquid fuel. This fuel is composed of a molten salt mixture containing fertile and fissile isotopes (see section 1.2). The innovative angle is that the salt serves as the coolant and at the same time, transfers the heat. The thermal energy from the nuclear fission is transferred in an intermediate heat exchanger into another liquid salt. A power cycle facility



images/MSFR-schematic-representation.PNG

Figure 1.1: Schematic representation of a Molten Salt Fast Reactor [6].

generates electricity from the heat. In order to continuously keep the reactor running, the fuel salt is extracted and cleaned in a chemical processing plant, where fission products are removed and the fissile concentration is adjusted.

The nuclear reactors in use today have multiple disadvantages in comparison with the new MSFR. One of the most dangerous risks is the meltdown of the reactor's solid core. In this situation, the core reaches such a high temperature that radioactive materials would break through all containment and leak into the environment. Radioactive contamination potentially leads to radiation poisoning of the population. Because a MSFR has a nuclear fuel that is already a molten liquid, no such accident could occur. Also, the MSFR does not operate at high pressure but at atmospheric pressure, excluding the chance of a possible explosion. If nonetheless a critical accident occurs, for instance when the power supply fails, due to the liquid nature of the fuel it could be drained away. Then, freeze plugs would melt as the liquid drains into multiple storage tanks, placed underneath the core.

Aside from safety aspects, a Molten Salt Fast Reactor has advantages concerning the efficiency and the sustainability. The temperature on which a MSFR operates is higher than for traditional reactors hence a higher thermodynamic efficiency can be realised while still having a low vapor pressure. Inside the reactor the fuel is constantly recirculating, thereby burning nearly all fuel. Whereas for current reactors the waste produced stays radioactive for about $2.5 \cdot 10^5$ years, the waste from a MSFR reaches natural levels already after a couple of centuries [1].

1.1.2 SAMOFAR

SAMOFAR (Safety Assessment of the MOlten Salt FAst Reactor) is a project where eleven European universities and research institutes cooperate to study the safety of the Molten Salt Fast Reactor (MSFR). It is one of the most prominent Research and Innovation projects in the Horizon 2020 Euratom research program. Research is done to achieve a breakthrough in nuclear safety and nuclear waste management and to make nuclear energy truly safe and sustainable [3].

1.2 Properties of the molten salt

Nearly all design choices of a MSFR are influenced by the characteristics of the liquid fuel. Only with the fluid's properties, the operation parameters (temperature and pressure) and the reprocessing scheme can be defined, which in turn have effect on all design choices. When choosing what mixture of the molten salt should be used, it must have a low melting point, low absorption cross-section, low radioactivity induced by radiation and it should be chemically stable. In order to determine the behaviour of the fuel in the reactor, the thermodynamic properties (density, viscosity, thermal conductivity and specific heat capacity) should be well-known.

The density of the fuel is determinative for the amount of neutrons. The viscosity is essential in knowing how the fuel will flow in the reactor, resulting in either a turbulent or a laminar flow. The flow of the fuel is a crucial factor in the heat transfer of the MSFR. For the determination of the storage tank's specifications, the specific heat capacity is important. Because for a high specific heat capacity, a large amount of energy can be stored in a relatively small tank. To obtain a good heat transfer, the thermal conductivity must be high.

Due to the fact that fluorides have a low melting point and a low capture cross section, they are considered as primary choice for the fuel. A fluoride salt at low temperatures is one of the most stable compounds [1]. However, when temperature increases, and when moisture is present, the vapours rapidly corrode the materials of the instruments. Whereas current devices are able to measure the thermal conductivity and the specific heat transfer of the fluoride mixture, the density and viscosity can not be measured. The current devices are unable to cope with the high temperature (between 500 and 1200 degrees Celcius [1]), radioactivity and corrosiveness of this material.

For the MSFR, a multi-component fluoride mixture can be used with ThF_4 , UF_4 and PuF_3 [15]. ThF_4 is represented by a ^{232}Th isotopes and is used as fertile material to breed ^{233}U . The fissionable UF_4 is necessary to control the redox potential of the fuel via the $\text{UF}_4 / \text{UF}_3$ ratio. PuF_3 (containing the ^{239}Pu isotope) only represents about 3 % of the salt and is a fissionable material. To gain further insight in what exact mixture can be used in a molten salt reactor, devices must be developed to measure its density and viscosity.

1.3 Ultrasonic wave method

The measurements of the density and the viscosity in this research will be done using the innovative idea of using ultrasonic waves. This way of measuring meets the conditions set by the temperature, radioactivity and corrosiveness of the material. The fact that only one device will be able to measure both the viscosity and the density at the same time, is an additional advantage.

The ultrasonic wave measurement technique uses a transducer that consists of a piezoelectric element that generates a short ultrasonic wave. Ideally, this transducer should transmit waves directly into the fluid. Then, the wave entering the fluid attenuates and the reflection is measured with the receiver. From this attenuation, the viscosity can be calculated. Research has been done on the use of this ultrasonic technique on low temperature fluids since 1949 [17, 18].

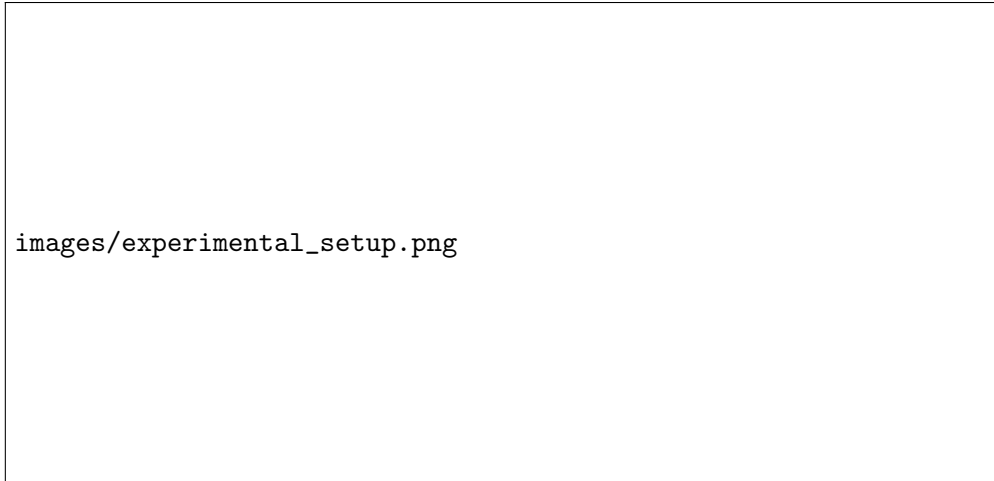


Figure 1.2: Overview of the experimental setup [1].

Unfortunately, since a the molten salt's temperature is too high and due to its radiation, this exact measuring apparatus can not be used for determining the liquid salt's characteristics. For temperatures exceeding the Curie temperature, the piezoelectric element becomes depolarised and can not be used anymore. Also, the gamma rays radiated by the fuel deteriorate the piezoelectric behaviour.

In order to prevent the piezoelectric transducer from depolarising, the waves are guided through a waveguide, into the fluid. Part of the wave reflects at the solid-fluid interface, influenced by the physical properties of the fluid (viscosity and density) and the waveguide (density and shear modulus). For the scope of this research, a rod will be used as the waveguide. Other waveguides (e.g. a strip) will not be considered here, as they already are currently being investigated by the SAMOFAR project.

When a longitudinal wave propagates through the waveguide, the density is determined directly from the reflection coefficient at the boundary of the fluid and the waveguide. Using air as a reference material, the density of the fluoride mixture can be determined. The viscosity can be calculated when the waveguide (buffer rod) is immersed in the fluoride salt. The waves propagate down through both the waveguide and the fluid and after reflection at the bottom of the fluid, they propagate back up. When the waves reach the top of the waveguide, they will be measured. Due to the fact that the waveguide is immersed in the salt, the wave attenuates. From this attenuation, eventually the viscosity is calculated, which will be explained in more detail in section 2.4. The experimental set-up is displayed in figure 1.2.

Within a fluid, only longitudinal (pressure) waves can exist. This is due to the fact that a fluid has no rigidity. Solid materials, like a buffer rod, have a high rigidity. This causes the presence of shear waves. In solids, pressure waves can become shear waves and vice versa due to mode conversion at the boundaries of the waveguide (see section 2.3). When the originally generated pressure waves convert into shear waves, they will travel at a slower rate. This is because the shear wave speed is lower than the pressure wave speed. This conversion of waves causes trailing echoes (spurious echoes).

The problem arises when measuring the viscosity. Because in order to calculate the viscosity, the attenuation of the wave when it propagates in the molten salt, must be measured. The unfortunate conclusion is drawn that the echo to be measured for determining the attenuating, comes in at about the same time as the trailing echoes [7].

1.4 Aim of this research

Since the measurement of the viscosity is deteriorated by the trailing echoes, these echoes ought to be reduced. The main goal of this research is to create models in COMSOL to optimise the reduction of trailing echoes. One way of doing this is tapering the buffer rod, as was recently studied by Oud [7]. For one geometry, the optimal tapering angle was determined to be 1.25 degrees. This research aims to find more tapering angles for other geometries. Another way of reducing the trailing echoes is by using buffer rods that have an irregular polygonal shape. Simulations will be done to verify this method.

In order to find the optimal simulation properties, different simulations will be done by varying the time step of the simulation and the mesh density. The outcome of these simulations are post-processed with Matlab and will be used for executing all the simulations to find the optimal tapering angles for different sizes of the waveguide.

Chapter 2

Theory of acoustic waves

Humans can hear sounds with frequencies from approximately 20 Hz up to 20,000 Hz. Ultrasound is a term used for sound waves with frequencies higher than the upper audible limit of human hearing. Ultrasound doesn't differ from 'normal' sound in its physical properties, except that it can't be heard by humans.

The definition of a wave is a self-sustaining propagation at a constant velocity without change of shape. Acoustic waves are described by the pressure field and velocity field. By disturbing a medium, a local pressure difference can arise causing acoustic waves. Due to this change in pressure, energy will start flowing through the medium.

Based on the qualitative differences in properties of a medium, a distinction between transmission media can be made. Matter is divided into three states: gas, liquid and solid. The most densely packed state is that of solid. Whereas the solid state is rigid, both the liquid and the gas state have no rigidity, meaning that they cannot resist deformation. The latter is important since a wave behaviour is predominantly determined by the medium the wave is propagating in.

Within a fluid, due to the fact that they do not have the ability to resist deformation, waves can only travel along the same axis in which the particle travels. Waves traveling in this direction are called longitudinal, pressure or compressional waves. In solids however, another type of waves exist, being the shear wave (transverse wave). Shear waves have a particle moving perpendicular to the propagating direction of the waves and therefore need a rigid medium. The two wave speeds are governed by two different types of moduli. The bulk elasticity modulus defines the longitudinal wave speed, while the shear elasticity modulus defines the shear wave speed.

This chapter not only presents multiple derivations but it will also define the notations used in the entire thesis.

2.1 Bulk waves in fluids

2.1.1 Acoustic wave equations

When assuming that the wave motions in the model are small perturbations, acoustic waves arise. This is the case for waves in a fluid, because velocity, density and deformation have only small changes. The relation between pressure and change in velocity is defined in Newton's second law of motion, by solving the equation of momentum. Newton's law can be expressed as [22]:

$$\nabla p = -\rho \frac{\partial \mathbf{v}}{\partial t}, \quad (2.1)$$

where p is the pressure and \mathbf{v} is the particle velocity vector. ρ is the density of the medium and t is the time. When variations in pressure are small, the relation between the applied pressure and the compression of the fluid is given by Hooke's law. The deformation of a fluid can be expressed by its compressibility (χ):

$$\frac{\partial p}{\partial t} = -\frac{1}{\chi} \nabla \cdot \mathbf{v}. \quad (2.2)$$

The minus sign indicates the inverse relation between pressure and change in displacement. Multiplying equation 2.2 by $\rho\chi \frac{\partial}{\partial t}$ and taking the gradient of 2.1 gives the (3D) wave equation for the pressure field [1]:

$$\nabla^2 \mathbf{p}(t) - \frac{1}{c^2} \frac{\partial^2 \mathbf{p}(t)}{\partial t^2} = 0, \quad (2.3)$$

where c represents the speed of the wave in the fluid. This equation is only valid for inviscid fluids. When incorporating the motion of the viscosity (μ) of the medium, the wave equation for viscous fluids is obtained:

$$\nabla^2 \mathbf{p}(t) - \frac{1}{c^2} \left(\frac{\partial^2 \mathbf{p}(t)}{\partial t^2} + \frac{3\mu}{3\rho} \frac{\partial(\nabla^2 \mathbf{p}(t))}{\partial t} \right) = 0. \quad (2.4)$$

2.1.2 Attenuation in a fluid

For the derivation of the viscosity of the fluid, the attenuation coefficient (α) will be used. Attenuation is the loss of energy due to dissipation by the viscous properties of a fluid. The amplitude of the waves thereby significantly decreased in a viscous fluid. For the derivation of the attenuation coefficient, the one-dimensional plane wave solution is considered [1]:

$$p(x, t) = p_0 e^{\pm i(kx - \omega t)}, \quad (2.5)$$

The wavenumber k is equal to $\frac{\omega}{c}$, where ω represents the angular frequency and where x is the distance travelled in the direction of the propagation of the wave. Inserting the expression of the plane wave (2.5) into the wave equation for viscous fluids (2.4) gives:

$$k = \pm \frac{\omega}{c} \frac{1}{1 + i\omega \frac{4}{3} \frac{\mu}{\rho c^2}} = \pm \beta - i\alpha, \quad (2.6)$$

where α is the attenuation coefficient and $c = \frac{\omega}{\beta}$ the phase velocity. Equation 2.6 can be solved by applying a Taylor expansion. This results in a solution for the attenuation coefficient, which is dependent on the viscous properties of the fluid [1]:

$$\alpha = \frac{2\omega^2 \mu}{3\rho c^3}. \quad (2.7)$$

2.2 Bulk waves in solids

In this section, the theory describing the behaviour of wave propagation in the bulk is presented. The derivation of the wave equation in a solid and the concept of mode conversion will be introduced with its consequences.

2.2.1 Stress and strain tensor

In order to derive the wave equations of a wave propagating through a solid, first the stress and strain tensors must be defined. In continuum mechanics it is common to express stress and strain in tensors. When applying a pressure on a solid, it will start to deform. This deformation could be either parallel or perpendicular to the force applied. In 1678, Robert Hooke stated a rule between extension and force. This rule, Hooke's law, gives stress as a linear function of strain. For small displacements, the stress σ is given by:

$$\sigma(\mathbf{u}) = C\epsilon(\mathbf{u}), \quad (2.8)$$

with the vector field \mathbf{u} being the three-dimensional displacement, the combination of the longitudinal and transverse displacement ($\mathbf{u} = \mathbf{u}_{\text{longitudinal}} + \mathbf{u}_{\text{transversal}}$). The strain vector is represented by $\epsilon(\mathbf{u})$. C is the elastic moduli tensor, which in this research is taken constant, due to the fact that isotropic media will be used. The stress matrix is given by:

$$\sigma(\mathbf{u}) = \begin{bmatrix} \sigma(u_{ii}) & \sigma(u_{ij}) & \sigma(u_{ik}) \\ \sigma(u_{ji}) & \sigma(u_{jj}) & \sigma(u_{jk}) \\ \sigma(u_{kj}) & \sigma(u_{kj}) & \sigma(u_{kk}) \end{bmatrix} \quad (2.9)$$

In this matrix the diagonal terms represent the longitudinal stresses and the off-diagonal terms are the shear stresses. When strain is small ($|\frac{\partial \mathbf{u}_i}{\partial x_i}| \ll 1$), the strain tensor ϵ can be linearised and written in gradient notation:

$$\epsilon(\mathbf{u}) = \frac{1}{2} (\nabla \mathbf{u} + (\nabla \mathbf{u})^T), \quad (2.10)$$

this formula states that two different strains are possible in solids, being the tensile and shear strain. These strains are mutually perpendicular and are displayed in figure 2.1.

For a two-dimensional isotropic material, formula 2.8 can be rewritten because the number of elastic constants (C in formula 2.8) reduces to two. This results in the simplified Hooke's law:

$$\sigma(\mathbf{u}) = \lambda(\nabla \cdot \mathbf{u})\mathcal{I} + 2\mu\epsilon(\mathbf{u}), \quad (2.11)$$

where \mathcal{I} is the identity matrix λ and μ are Lamé parameters. They can be expressed in Young's modulus (E) and the poisson ratio (ν). Young's modulus indicates the stiffness of a solid, describing how much force is needed for a certain deformation. The Poisson ratio is the ratio of transverse strain to axial strain, it is a measure of the compressibility of a solid. The equations for the Lamé parameters become:

$$\mu = \frac{E}{2(1 + \nu)} \text{ and } \lambda = \frac{E\nu}{(1 + \nu)(1 - 2\nu)}. \quad (2.12)$$

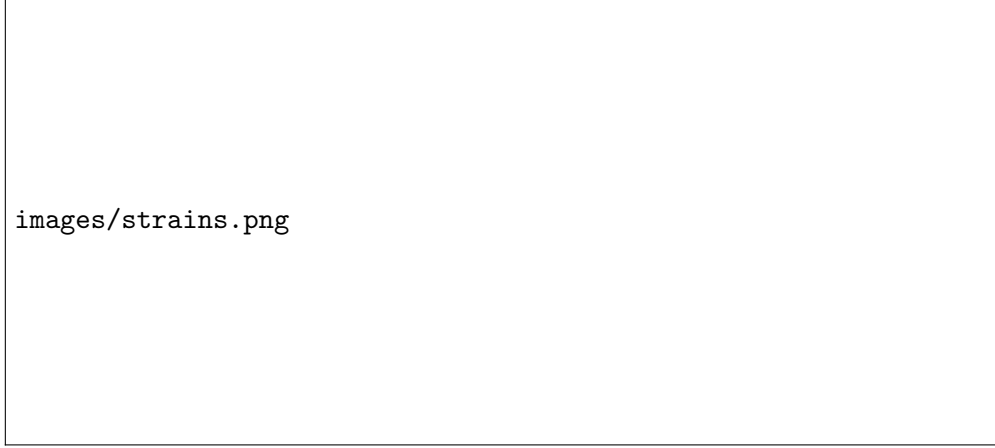


Figure 2.1: Tensile and shear strain for a cube [14].

2.2.2 Elastic wave equations

For the derivation of the elastic wave equations, the linear momentum be conserved, giving:

$$\rho \left(\frac{\partial \mathbf{v}}{\partial t} + \mathbf{v} \cdot \nabla \mathbf{v} \right) - \nabla \cdot \sigma(\mathbf{u}) = \mathbf{f}, \quad (2.13)$$

where $\left(\frac{\partial \mathbf{v}}{\partial t} + \mathbf{v} \cdot \nabla \mathbf{v} \right)$ is the material derivative of velocity [22] and ρ represents the density of the material. For the scope of this research, the source function (f) is non-existing. In the situation where deformations are small, $\mathbf{v} \cdot \mathbf{v} \approx 0$ and $\mathbf{v} \approx \frac{\partial \mathbf{u}}{\partial t}$. Modifying equation 2.13 with these simplifications gives:

$$\rho \frac{\partial^2 \mathbf{u}}{\partial t^2} = \nabla \cdot \sigma(\mathbf{u}), \quad (2.14)$$

Combining equation 2.14 with Hooke's law, equation 2.11, gives the Navier Cauchy equation (in vector notation):

$$(\lambda + \mu) \nabla (\nabla \cdot \mathbf{u}) + \mu \lambda^2 \mathbf{u} = \rho \frac{\partial^2 \mathbf{u}}{\partial t^2}. \quad (2.15)$$

To clearly derive the longitudinal and shear wave speed, it is convenient to define the dilation of the solid by $\nabla \cdot \mathbf{u} = \Delta$ and the rotation vector ω by $\omega = \nabla \times \mathbf{u}$, resulting in:

$$(\lambda + \mu) \nabla \Delta - 2\mu \nabla \times \omega = \rho \frac{\partial^2 \mathbf{u}}{\partial t^2}. \quad (2.16)$$

2.2.3 Longitudinal wave speed

For the shear waves, the particles of the medium move perpendicular to the axis of the propagation of the wave. Thus, it has no divergence: $\nabla \cdot \mathbf{u}_{\text{transversal}} = 0$. This could be exploited to define the longitudinal wave speed. The divergence of equation 2.15 yields

$$(\lambda + \mu) \nabla \cdot \nabla (\nabla \cdot \mathbf{u}) + \mu \nabla \cdot \lambda^2 \mathbf{u} = \nabla \rho \cdot \frac{\partial^2 \mathbf{u}}{\partial t^2}, \quad (2.17)$$

combining this with $\nabla^2 = \nabla \cdot \nabla$, $\nabla \cdot (\nabla^2 \cdot \mathbf{u}) = \nabla^2(\nabla \cdot \mathbf{u})$ and $\nabla \cdot \mathbf{u} = \Delta$ results in

$$\nabla^2 \Delta = \frac{\rho}{\lambda + 2\mu} \frac{\partial^2 \Delta}{\partial t^2}. \quad (2.18)$$

For longitudinal waves, the wave speed (physically being the change in volume) then is

$$c_l = \sqrt{\frac{\lambda + 2\mu}{\rho}}. \quad (2.19)$$

2.2.4 Shear wave speed

The derivation of the shear wave speed goes in a similar way, where instead of taking the divergence, the operation of curl is performed. Since $\nabla \times \mathbf{u}_{\text{longitudinal}} = 0$, this results in

$$(\lambda + 2\mu) \nabla \times \nabla \Delta - 2\mu \nabla \times (\nabla \times \omega) = \rho \nabla \times \frac{\partial^2 \mathbf{u}}{\partial t^2}. \quad (2.20)$$

Combining this with $\omega = \frac{1}{2}(\nabla \times \mathbf{u})$ and $\nabla \cdot (\nabla \times \mathbf{u}) = 0$ gives

$$\nabla^2 \omega = \frac{\rho}{\mu} \frac{\partial^2 \omega}{\partial t^2}. \quad (2.21)$$

From this, the wave speed of shear waves can be deducted:

$$c_s = \sqrt{\frac{\mu}{\rho}}. \quad (2.22)$$

2.3 Wave characteristics at boundaries

When taking a closer look at the behaviour of waves at boundaries of different materials, mode conversion can be seen. When elastic waves hit a boundary under an angle, the reflected and transmitted wave are converted in two different types of waves. Incoming longitudinal waves will end up as longitudinal waves and shear waves. Shear waves can also transform back into longitudinal waves. To describe the behaviour at boundaries, the wave equation presented above will need boundary conditions.

The behaviour at the boundaries of elastic waves is comparable with that of (optical) light propagating from one material to another. The incoming wave will refract and thus the outgoing wave will have a different angle with respect to the normal. This is graphically displayed in figure 2.2 and is defined by Snell's law (2.23) as

$$\frac{\sin(\theta_1)}{\sin(\theta_2)} = \frac{c_1}{c_2} = \frac{k_2}{k_1}, \quad (2.23)$$

where c_1 and k_1 are the wave speed and the wave number, respectively, of the incoming wave. c_2 and k_2 are the properties of the transmitted wave.



Figure 2.2: Refraction of light at the interface between two media of different refractive indices, with $n_2 > n_1$. Since the velocity is lower in the second medium ($v_2 < v_1$), the angle of refraction θ_2 is less than the angle of incidence θ_1 [23].

2.3.1 Solid-liquid interface

When a wave propagating in a solid hits an interface where a solid and liquid meet, part of the wave reflects and another part transmits into the liquid. At this interface the wave numbers must be the same, $k_1 = k'_1 = k_2$, where k'_1 is the wave number of the reflected wave. For a longitudinal wave at a solid-liquid interface, the pressure and normal displacement must be continuous at both sides. The amplitudes (A) of the longitudinal waves are defined by this boundary condition, being $A_1 + A'_1 = A_2$. With this, the reflection coefficient (R) and transmission coefficient (T) are defined as

$$R = \frac{A'_1}{A_1} \text{ and } T = \frac{A_2}{A_1}. \quad (2.24)$$

Because the normal displacement is dependent on the angle between propagation of the wave and the normal, the angles describing the direction of the incoming (θ_1), the reflected (θ'_1) and the transmitted (θ_2) are given by

$$\nu_1 \cos(\theta_1) - \nu'_1 \cos(\theta'_1) = \nu_2 \cos(\theta_2), \quad (2.25)$$

where ν is the particle velocity, defined as $\nu \equiv \frac{p}{\rho c}$. Because the angle of incidence is equal to the angle of the reflected wave, $\theta_1 = \theta'_1$, equation 2.24 can be rewritten as [1]

$$R = \frac{\rho_2 c_2 \cos(\theta_1) - \rho_1 c_1 \cos(\theta_2)}{\rho_2 c_2 \cos(\theta_1) + \rho_1 c_1 \cos(\theta_2)} \text{ and } T = \frac{2\rho_2 c_2 \cos(\theta_1)}{\rho_2 c_2 \cos(\theta_1) + \rho_1 c_1 \cos(\theta_2)}. \quad (2.26)$$

The calculation of the density of a fluid requires that the acoustic impedance (Z) must be calculated. The acoustic impedance is the ratio between the pressure (p) and the velocity of the particle in a

medium (v), defined as $Z = \frac{p}{v} = \rho c$. With the definition of the acoustic impedance, 2.26 can be rewritten as

$$R = \frac{Z_2 \cos(\theta_1) - Z_1 \cos(\theta_2)}{Z_2 \cos(\theta_1) + Z_1 \cos(\theta_2)} \text{ and } T = \frac{2Z_2 \cos(\theta_1)}{Z_2 \cos(\theta_1) + Z_1 \cos(\theta_2)}. \quad (2.27)$$

2.3.2 Solid-Air Interface

For this research, waves will travel through a waveguide surrounded by air. The acoustic impedance of metals is much greater than that of air. Thus, for the scope of this research, the transmission at the solid-air interface is neglected and only reflection is investigated. Upon reflection, a part of the wave converts to the other mode type, and the other part remains unchanged. The reflection coefficients are obtained when combining two boundary conditions with Hooke's law for isotropic solids and Snell's law, equation 2.11 and 2.23. The boundary conditions are that on the interface between two media there is no normal stress and no tangential stress. The reflection coefficients become [19]:

$$R_{L \rightarrow L} = \frac{\sin(2\theta) \sin(2\theta_l) - (c_l/c_s)^2 \cos^2(2\theta)}{(2\theta_s) \cos(2\theta_l) + (c_l/c_s)^2 \cos^2(2\theta)}, \quad (2.28)$$

$$R_{L \rightarrow S} = \frac{2(c_l/c_s) \sin(2\theta_l) \cos(2\theta)}{(2\theta_s) \cos(2\theta_l) + (c_l/c_s)^2 \cos^2(2\theta)}, \quad (2.29)$$

$$R_{S \rightarrow S} = -\frac{\sin(2\theta) \sin(2\theta_l) - (c_l/c_s)^2 \cos^2(2\theta)}{(2\theta_s) \cos(2\theta_l) + (c_l/c_s)^2 \cos^2(2\theta)}, \quad (2.30)$$

$$R_{S \rightarrow L} = \frac{2(c_l/c_s) \sin(2\theta) \cos(2\theta)}{(2\theta_s) \cos(2\theta_l) + (c_l/c_s)^2 \cos^2(2\theta)}, \quad (2.31)$$

where $R_{L \rightarrow L}$ is the reflection coefficient from longitudinal to longitudinal waves and where $R_{L \rightarrow S}$ represents the reflection coefficient from longitudinal to shear waves. $R_{S \rightarrow S}$ and $R_{S \rightarrow L}$ are the reflection coefficients from shear to shear and shear to longitudinal. A further explanation of mode conversion is presented in section 2.6. For the reflection coefficients, θ_s and θ_l are the angles with respect to the normal, respectively, of the shear waves and of the longitudinal waves. The wave speeds of the shear and longitudinal waves are denoted as c_s and c_l .

2.4 Calculations of thermodynamic properties

2.4.1 Density calculation

As presented in section 2.3.1, the density of a fluid can be calculated using the reflection coefficient. The density will be calculated for the case that the longitudinal waves propagates perpendicular to the solid-fluid interface. The density of the fluid (ρ_2) is calculated by [1]

$$\rho_2 = \frac{Z_2(1 - R)}{c_2(1 + R)}. \quad (2.32)$$

For the waveguides used in this research, the acoustical impedance (Z_2) is known. Thus, the variables to be determined are the reflection coefficient from solid to fluid (R) and the speed of the wave in the fluid (c_2). The speed of the wave in the fluid can be determined by measuring the echoes of ultrasonic waves that are propagated up and down the waveguide. The initial pulse partially reflects back into the waveguide and partially transmits into the fluid. The time at which the reflected wave returns is called t_1 . The transmitted wave reflects at the bottom of the fluid

and then transmits (partially) back into the waveguide. This pulse then returns to the top of the waveguide at time t_2 . Exploiting this time-delay and using the known distance that the wave has to travel within the fluid (l), the speed of the wave in the fluid can be calculated as

$$c_2 = \frac{2l}{t_2 - t_1}. \quad (2.33)$$

The bottom end of the solid waveguide is in contact with some other material. The reflection coefficient of the pulse between these materials is dependent on the acoustic impedance of both materials. In order to calculate the other unknown parameter R , measurements can be done by varying the material with which the end of the waveguide is in contact. The intensity of a pulse does not only change on an interface between media, it also changes due to attenuation in a waveguide. This attenuation is dependent on the distance the wave travels in the waveguide. To quantify this attenuation, a reference material can be used. When the waveguide is in contact with a reference material, the intensity (A_{ref}) is given as

$$A_{ref} = A_0 e^{-\alpha_{waveguide} 2l_{waveguide}} R_{ref}, \quad (2.34)$$

where $\alpha_{waveguide}$ represents the attenuation coefficient of the waveguide and where $l_{waveguide}$ is the length of the waveguide. In the same way, the intensity of a pulse can be given, when it is in contact with a fluid, as

$$A_{fluid} = A_0 e^{-\alpha_{waveguide} 2l_{waveguide}} R. \quad (2.35)$$

A_{fluid} and A_{ref} can be measured and R_{ref} can be calculated with equation 2.27. The reflection coefficient (R), from which the density of the fluid can be calculated, is given by

$$R = \frac{A_{fluid}}{A_{ref}}. \quad (2.36)$$

For the calculation of the viscosity of the fluid, equation 2.7 is rewritten into

$$\mu = \frac{3\alpha_{fluid}\rho_{fluid}c_{fluid}^3}{2\omega^2}. \quad (2.37)$$

Due to the fact that the angular frequency (ω), the density of the fluid (ρ_{fluid}) and the wave speed inside the fluid (c_{fluid}) are known, only the attenuation coefficient (α_{fluid}) must be found. Now, the intensities of pulses that propagate through both the waveguide and the fluid have to be measured. The intensity of the reflected pulse is approximated by

$$A_{fluid,depth} = A_0 e^{\alpha_{solid} 2l_{waveguide}} (1 - R)^2 e^{-\alpha_{fluid} 2l_{depth}}, \quad (2.38)$$

where l_{depth} is the depth a waveguide is immersed in the fluid to be investigated. To calculate the viscosity, the attenuation coefficient can be found by varying the immersion depth (l_1 and l_2). The attenuation can be calculated by

$$\alpha_{fluid} = \frac{1}{2(l_2 - l_1)} \ln \left(\frac{A_{fluid,l_1}}{A_{fluid,l_2}} \right). \quad (2.39)$$

This method is validated in a study of Prasad, Balasubramaniam, Kannan and Geisinger [11], where it gave the viscosity of molten glass within 5 percent error with NIST standard log viscosity values.

2.5 Explanation measurement plot

The measurements of the stress on the top of the wave front look like figure 2.3. In the plot, the initial wavefront is measured, caused by a vibration of the transducer. Then, some time passes where the top of the plot is still vibrating a little due to the initial displacement. After about $5 \cdot 10^{-5}$ seconds, the wave is propagated down and back up the buffer rod, where it is measured by the transducer. This reflection is called the first reflected wavefront. Shortly after, the trailing echoes are measured. Because mode conversion occurs multiple times, multiple peaks are measured for the trailing echoes. When the buffer rod is in contact with a fluid, the area in the plot where the trailing echoes are measured, will be the same as the area where the reflected wavefront from the fluid will be measured.

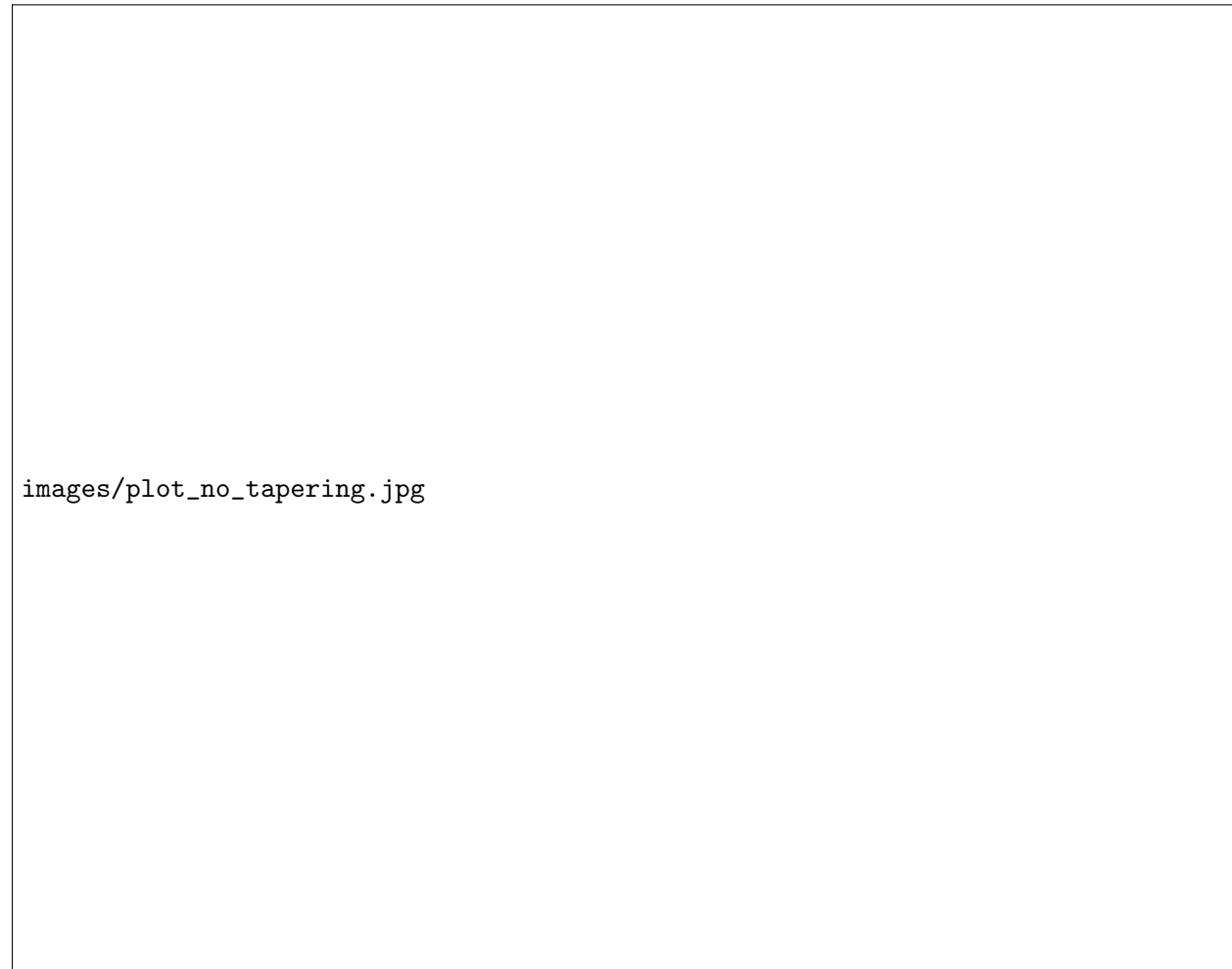


Figure 2.3: Typical ultrasonic pulse-echo response for a copper buffer rod with a length of 150 mm.

2.6 Trailing echoes

As a result of the mode conversion, trailing- or spurious echoes arise [8]. This happens when mode conversion takes place twice, first from the longitudinal to shear waves and subsequently from shear to longitudinal. The angle with respect to the normal under which shear waves are mainly formed, is depending on the material properties. The trailing echoes reduce the signal-to-noise ratio, making it necessary to optimise the system and reduce these trailing echoes.

Recent studies by Froeling and Oud showed that the trailing echoes can be simulated in COMSOL. In this section some of their results will be presented. Oud was trying to increase the signal-to-noise ratio to eventually create a set-up that could accurately measure the density and viscosity of (high temperature) fluids.

2.6.1 Wave propagation simulation in COMSOL Multiphysics

The three probable causes for spurious echoes are head waves, longitudinal waves and radiated edge waves. To verify that COMSOL Multiphysics can simulate an ultrasonic wave propagating through a waveguide, a 2-dimensional axial symmetric model has been made [4]. In the model, the top boundary (left boundary in figure 2.4) has a prescribed displacement along the axis of the rod. The wave packet used is a sinusoidal wave of 2 MHz, multiplied by a Gaussian window. The buffer rod is 83 mm long and 10 mm wide. A plot of an ultrasonic wave propagating through a copper buffer rod is displayed in figure 2.4.

2.6.2 Head waves

On the left side, the prescribed displacement wave is not applied to the entire width of the rod. Due to the fact that the transducer does not cover the entire top edge of the rod, the wavefront propagates over nearly the whole width, perpendicular to the axis of the rod. The displacement of the particles is in the direction in which the wave is propagating. The finite diameter causes the particles to collide with the edges, resulting in a reflection of longitudinal and shear waves. When the waves propagates it can be seen that the angle of incidence of the longitudinal waves is almost 90 degrees. The angle of of the shear wave is measured to be around 60 degrees with respect to the normal. This measurement is in accordance with equation (2.23) when calculating the longitudinal and shear wave speed of copper.

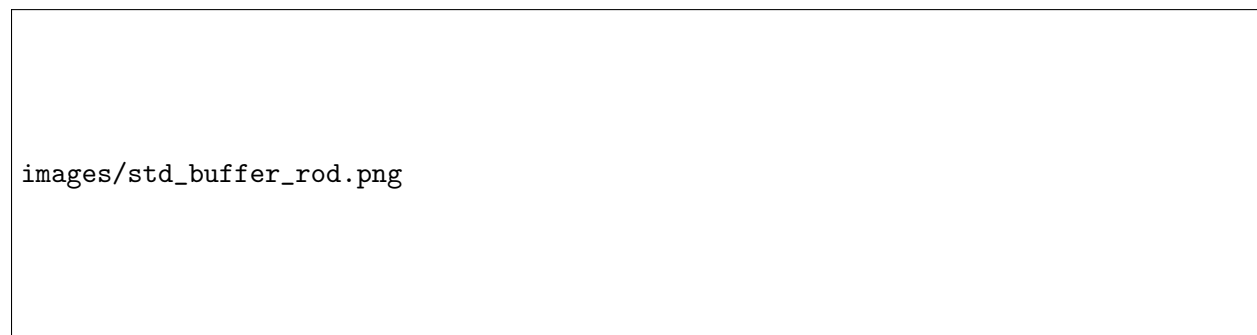


Figure 2.4: Propagation of ultrasonic waves ($f=2$ [MHz] in a copper buffer rod at $t = 2.4 \cdot 10^5$ [s]. The simulation consists of four types of waves, including the spurious echoes. [4]

The waves that are a result of this conversion of the longitudinal to the shear waves are not normal shear waves, they are called head waves. Although the waves are shear waves, the location at which they are generated travel at the speed of the longitudinal waves. The location where mode conversion takes place is where the initial longitudinal waves hit the edge of the rod. This location moves along the axis of the rod with the longitudinal wave speed. The head waves coming from the edges of the rod eventually form a crossing shape.

2.6.3 Conversion from shear waves to longitudinal wavefront

After the head waves have formed a cross, they strike the opposite edge of the rod, where they again will be reflected. The incoming, then, are partly reflected and partly converted back into longitudinal waves. The resulting longitudinal wavefront propagates parallel to the initial wavefront.

The produced longitudinal wavefront will have a significant intensity, in the order of the intensity of the initial wavefront. This is the result of the continuous production of head waves which eventually convert back into longitudinal waves. Because of the uniform diameter of the rod, the longitudinal wavefront is concentrated on a fixed distance behind the initial wavefront, having a great contribution to spurious echoes.

2.6.4 Radiated edge waves

Ideally, the transducer should generate purely longitudinal waves propagating along the longitudinal axis of the rod. However, in an experimental set-up, this is not always the case. Sometimes, the piezo-electric elements are smaller than the diameter of the rod. As a side effect, the transducers then produce shear edge waves. The velocity of these waves is about half the wave speed of the longitudinal wave. This is displayed in figure 2.5b, where to the left of the head waves, the edge waves can be seen.

The incident angle of these shear waves at the edges of the rod is dependent on the ratio of the width of the transducer over the width of the buffer rod. Figure 2.6 shows that when this ratio is high, less shear waves are produced than when that ratio is low. Since the angle of incidence of the radiated shear waves are changing continuously, no structural behaviour is observed and the noise is therefore considered as random. It does not have a great contribution to trailing echoes.



(a) Schematic representation of ultrasonic transducer in contact with the buffer rod [10]

(b) Plot of radiated edge waves, consisting of longitudinal and shear waves [4]

Figure 2.5: Schematic representation with its resulting displacement plot when ratio of transducer width over the diameter of the rod is 0.3.

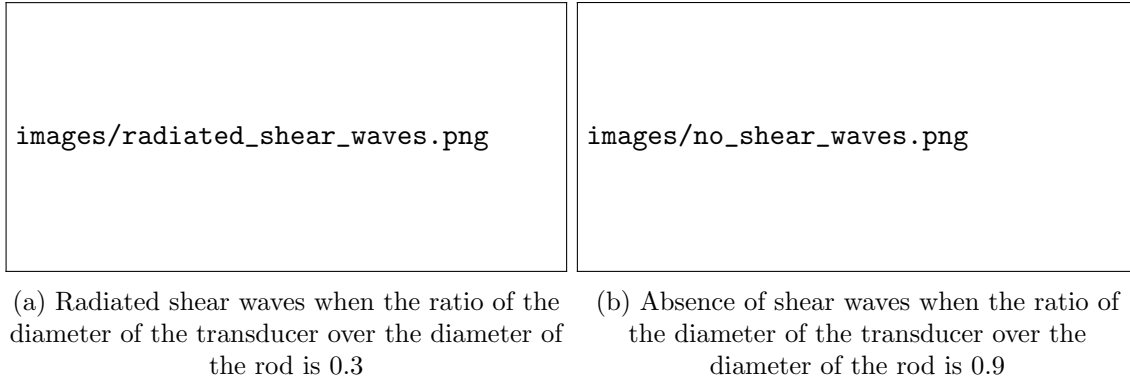


Figure 2.6: The contribution of trailing echoes is lower for a small diameter of the transducer than for a higher diameter [4].

2.7 Reducing trailing echoes

2.7.1 Buffer rod tapering

After the work of Froeling, the effect of tapering the buffer rod was investigated by Oud. This idea was based on the work done by Ihara, Tsuzuki and Kikura [8] and on the work of Pezant, J. Michaels and T. Michaels [9]. These studies showed that it is possible to increase the signal-to-noise ratio (SNR) by double tapering a buffer rod. In his thesis, Oud showed that it is possible to simulate the reduction of the spurious echoes in COMSOL. The configuration where the rod was tapered on both ends gave better results than when only a single tapering from top to bottom was used. How this works will be explained in section 2.7.1.

Only for one specific geometry, with a length of 83 mm and width 20mm, simulations were performed for rods with tapering angles between 0 and 1.75 degrees. The comparison of the straight and tapered rod is displayed in figure 2.7. Oud's recommendations were to check for different geometries what the ideal angle would be to enhance the signal-to-noise ratio.

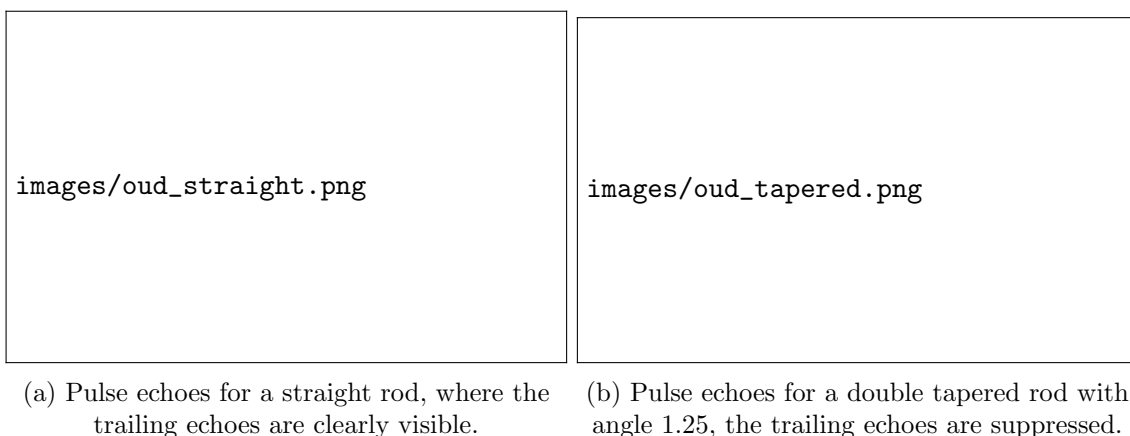


Figure 2.7: Pulse echoes, measured at the transducer's location, for a straight and tapered buffer rod of 83 mm long and 20 mm wide. The measurements were done with a pulse of 2 MHz. [7].

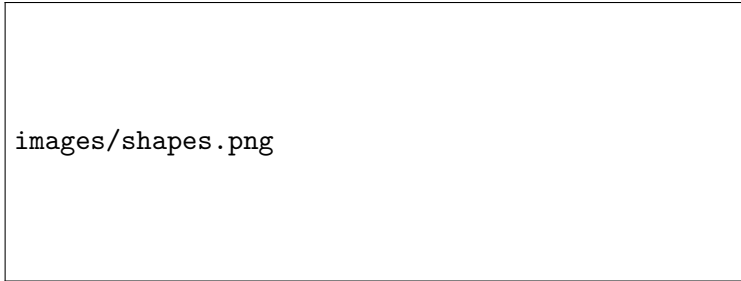


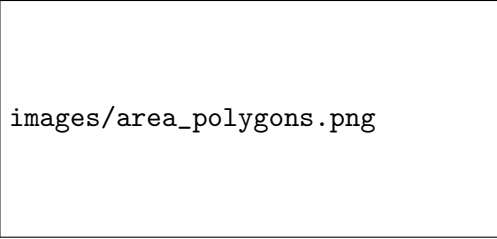
Figure 2.8: Three-dimensional simulation model for some polygonal buffer rods [10].

2.7.2 Polygonal buffer rods

Research done by Foudzi (2014) showed that it is also possible to use polygonal buffer rods as an alternative method to reduce the trailing echoes and result in improving the SNR. Instead of using a cylindrical buffer rod, the idea is to use a polygonal rod whose normal sectional shape is a polygon. This could be a triangle, square, pentagon etc. [10]. To prove this effectiveness, the idea has been examined numerically and experimentally. Triangles, pentagons and heptagons have sides that are not parallel to any of the other sides. With three-dimensional numerical simulations, they were proven to cause less interferences among mode converted waves in the rod. This technique enhances the SNR partly, but still less spurious echoes are required for a decent viscosity measurement apparatus. Trailing echoes are generated by the interference of the waves due to the bilateral symmetry shape of the odd polygons. Figure 2.8 shows the cross-sectional shapes of the buffer rod and their 3D simulation model.

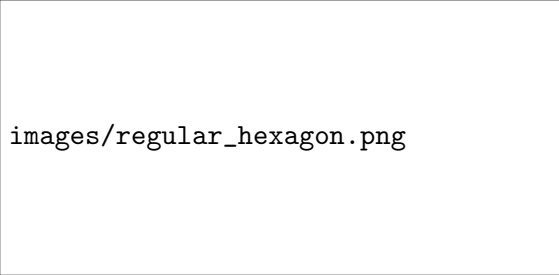
The polygons with an odd number of sides (odd-n polygons) were found to give better results than the polygons with even number of sides (even-n polygons). Since none of the odd-n polygons have parallel sides, less trailing echoes were generated and the SNR was improved. The amplitude of the first trailing echo for odd-n polygons has been proven to gradually decrease when increasing the number of sides. This is due to the fact that the area where such trailing echoes could be formed, decreases. It was found that the biggest area for a possible generation of trailing echoes is that of a triangle. This idea is shown for odd-n polygons in figure 2.9.

To obtain an ever high SNR, Foudzi's idea was to use irregular polygons, where at least one of the vertices of the polygon is distorted. This influences the symmetry of the polygon, reducing the trailing echoes. How distorting vertices works is illustrated in figures 2.10 and 2.11.



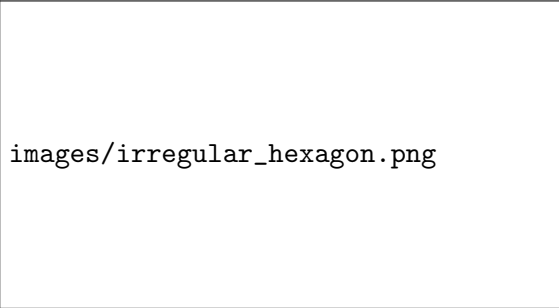
images/area_polygons.png

Figure 2.9: Comparison of the area that contributes to the generation of the first trailing echoes between triangle, pentagon and heptagon. [10]



images/regular_hexagon.png

Figure 2.10: Mechanism to generate the first trailing echo for a regular hexagon. It is clearly visible that the echoes are focused in the middle of the rod. [10]



images/irregular_hexagon.png

Figure 2.11: Mechanism to generate the first trailing echo for an irregular hexagon. The focusing of the echoes is not as intense as for the regular hexagon. [10]

Chapter 3

Simulation model

The simulations done for this research were done in COMSOL Multiphysics. COMSOL Multiphysics is a cross-platform finite element analysis, solver and multiphysics simulation software. For the ultrasonic wave propagation through a solid rod, the Solid Mechanics module will be used. This chapter will clarify as well as possible the decisions made in simulating the problem.

3.1 General properties in COMSOL

3.1.1 Wave packet

In the beginning process of modelling, definitions and parameters are assigned. The prescribed displacement that will be used is a sinusoidal signal multiplied with a Gaussian window, plotted in figure 3.1.

3.1.2 Boundary conditions

There are two important boundary conditions. One describes the behaviour of the boundary on which the transducer is acting, the other describing all remaining boundaries. A prescribed displacement is applied in the direction of the longitudinal axis of the rod, where the transducer is in contact with the boundary. Equation 3.1 gives the displacement on the top surface of the buffer rod.

$$u = u_{0,z} = -w_0 \cdot \cos(2\pi f_0) \cdot e^{-\frac{1}{2} \left(\left((t-t_{delay}) \cdot \frac{NP \cdot t_{pulse}}{2} \right) \cdot \frac{6}{NP \cdot t_{pulse}} \right)^2}, \quad (3.1)$$

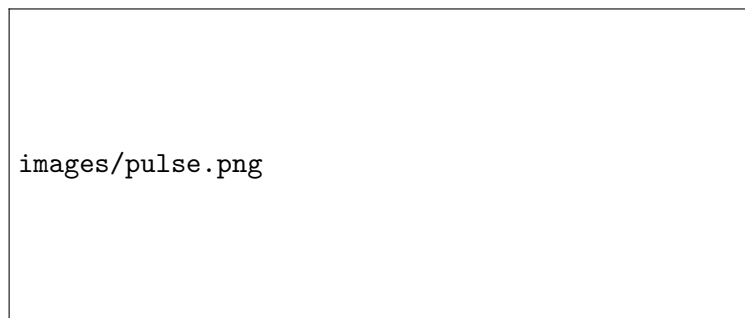


Figure 3.1: Pulse applied on edge of buffer rod, consisting of an infinite sine function multiplied by a Gaussian window.

where w_o represents the amplitude, f_0 the frequency, NP the width of the Gaussian window, t_{pulse} the period of the wave and where t_{delay} is used to delay the signal and to make sure the entire pulse response will be displayed in the plots. All other boundaries are assumed to be free boundary conditions, because there, the surrounding air is assumed to be interpreted and simulated as vacuum. This eliminates all transmissions, so only reflections will be seen in the results.

3.1.3 Dimensions and size

For simulating the buffer rod as a cylinder, a 2-dimensional axial symmetric model is made. The buffer rod has a length of 150 mm and a width varying from 20 to 40 mm. Since, as discussed in section 2.7.2, not only cylindrical buffer rods will be studied, it will be necessary to make 3D models. The amount of elements in the mesh will greatly increase because the mesh expands from a flat surface to a 3D volume. For obtaining the same accuracy with a buffer rod of the same size as for the 2D simulations, the computation time will be much more expensive. To avoid the simulations running for multiple days, the size of the buffer rod is decreased to 100 mm long and 25 mm wide.

3.1.4 Study type

In order to visualise the propagation of the wave, a time-dependent solver will be used. The time interval over which it will be calculated is at least $\frac{2L}{c_l}$, which is the time the ultrasonic wave takes to propagate up and down the buffer rod. No special solvers are used in the simulations, everything is calculated by the default solvers of COMSOL Multiphysics.

3.1.5 Materials

Precedent researchers did their simulations for copper only. In the next chapter simulation for both copper and for titanium are presented. The choice for these materials is that for copper, experiments are already done and for titanium, the software DISPERSE can verify the simulations. This is done by comparing the velocity calculated by DISPERSE with the velocity obtained by post-processing the results of the simulations. The materials that will be used are from the COMSOL materials library. The comparison between materials will be done using a Material Sweep, which is a function in COMSOL Multiphysics.

3.1.6 Measuring in COMSOL

In COMSOL there are multiple ways to measure the behaviour of the ultrasonic wave. To simulate a measurement that behaves like the transducer would in the real experimental setup, the surface integral is calculated at every time point. In structural mechanics, there are multiple ways stress can be measured. The measured quantity for the wave intensity in the simulations is the second Piola-Kirchhoff stress (material stress). This stress measurement is defined along the material axis and measures the stress with respect to the original cross-sectional area of the solid [24].

3.2 Discretisation of simulation model

The propagation of ultrasonic waves through a buffer rod is done with a finite element method and is a time-dependent problem. It is solved by dividing the time-domain in small time-steps. Not only the time-domain, but also the spatial domain is divided into small spatial steps. This discretisation is done by meshing the model. The accuracy of simulations is enhanced by narrowing the mesh-size and by reducing the time-steps. The downside of this is that the computation time increases, because more steps will have to be calculated. Generally, the Nyquist-rate defines that the size of one mesh element must be at most half the wavelength of the propagating wave. Equivalently, the time-step size should be smaller than half the period of the highest frequency wave.

3.2.1 Literature review on meshing

An important factor for obtaining an accurate result is the mesh-size of the model. For 2D-axial symmetric models, there is a simple way for describing the mesh density. A quadrilateral mesh can be used where the length of one element in the mesh (h) is determined as:

$$h = \frac{\lambda_l}{N}, \quad (3.2)$$

where λ_l is the longitudinal wavelength and where N represents the number of elements per wavelength. For ultrasonic wave simulations, the number of elements used in literature ranges from $N = 5$ up till $N = 12$.

3.2.2 Meshing in the simulations

The results from the mesh convergence plot in Oud's study were not completely satisfying. The fluctuating value of the error, when increasing the mesh density, could not be perfectly explained. Thus, the meshing of the buffer rod simulation will be revised. With the help of an advanced Matlab script, the peaks of the echoes will be detected more carefully and thereby the results are expected to be more accurate.

3.2.3 Literature review on time-stepping

The time-step is determined by the Courant–Friedrichs–Lewy (CFL) number. In the simulations, the time-step is given by:

$$\Delta t = \frac{h \cdot CFL}{c_l}, \quad (3.3)$$

where h is the length of one mesh element (eq. 3.2) and where c_l is the longitudinal wave speed. One study concludes that $CFL = 0.2$ results in accurate simulations with a reasonable computation, another study shows that $\Delta t = 1/100f$ gives the optimal result [13], where f is the frequency. This is equivalent to $CFL = \frac{N}{100}$. In order to make a stable calculation, the time step can also be chosen according to the von Neumann stability criterion:

$$\Delta t = \frac{h}{\sqrt{c_l^2 + c_s^2}}. \quad (3.4)$$

This gives for copper, with c_l and c_s around 4600 and 2300 m/s, a Courant number of 0.8. Oud and Froeling chose for their simulations a Courant number of 0.2. However, this time-step was not

used throughout their entire simulation. They only calculated the initial time-step and thereafter they let COMSOL converge to a time-step.

3.2.4 Time stepping in the simulations

Section 4.2 will present results for different values of the CFL-number and from that, a conclusion will be drawn. This CFL-number will be used throughout the thesis. In contrast to Oud's and Froeling's research, for this thesis a fixed time-stepping will be used. This is because for further research it is desirable to do spectral analysis of the signal, for which a fixed time-step is required.

Chapter 4

Results and discussion

This chapter describes all results obtained from the simulations done in COMSOL Multiphysics 5.2a. The results presented here are post-processed using Matlab. Initially, the relation between mesh density and accuracy is evaluated, followed by the optimisation of the time-stepping. The optimisation of these parameters will be used to eventually do all the other simulations.

4.1 Mesh density


For the 2-dimensional axial symmetric buffer rod, simulations are done to optimise the mesh density settings. Simulations are repeated when changing the number of mesh elements per wavelength. The accuracy is tested by calculating the propagation speed of the wave, calculated using a script in Matlab (can be found in appendix B). The mesh convergence plot is shown in figure 4.1. The error (e) is calculated with:

$$e = 100 \cdot \text{abs} \left(\frac{c_{sim.} - c_{theor.}}{c_{theor.}} \right), \quad (4.1)$$

where $c_{sim.}$ is the simulated wave speed and where $c_{theor.}$ is the theoretical wave speed in copper (4600 m/s). The mesh convergence plot shows that from $N = 8$ and higher the error of the wave speed becomes lower than 1%. This value will be used for the simulations of the buffer rod.


4.2 Time stepping

For determining the optimal time stepping, the effect of changing time steps is evaluated. For a buffer rod with a length of 150 mm and a diameter of 25 mm, the pulse echoes are measured. The model is simulated by varying the time step in the Time-Dependent Solver. The accuracy of the time-stepping ($\Delta t = \frac{h \cdot CFL}{c_l}$) increases when the Courant number decreases. For the simulations, the mesh density was set to $N = 8$, as was derived as optimal in section 4.1. A superposition of some pulse echoes for different Courant numbers is shown in 4.3. The plot shows that a decrease of the Courant number results in a shift in time of the first reflected peak. As for optimising the number of elements per wavelength, for the time discretisation the wave speed is measured as well. The convergence of for the time-stepping is shown in 4.2. It can be concluded that a Courant number of 1/10 gives accurate results. For this value, the calculation time was 30 minutes, which is reasonable. Thus, for the rest of the research in the sections below, this value will be used to define the time step of the Time-Dependent Solver.



images/mesh_convergence_plot.png

Figure 4.1: Mesh convergence plot of an ultrasonic wave propagating through a copper buffer rod, simulated in COMSOL.



images/cfl_convergence.png

Figure 4.2: Time stepping convergence plot of an ultrasonic wave propagating through a copper buffer rod, simulated in COMSOL

images/CFL_normal_zoomed.png

Figure 4.3: Pulse response for different values of the CFL-number, for a rod of 150 mm long and 25 mm wide.

Table 4.1: Results of the simulations done for different Courant numbers.

Courant number	1	1/2	1/5	1/8	1/10
time step [s]	$6.230 \cdot 10^{-8}$	$3.120 \cdot 10^{-8}$	$1.246 \cdot 10^{-8}$	$7.788 \cdot 10^{-8}$	$6.230 \cdot 10^{-9}$
Longitudinal wave speed [m/s]	4537.6	4585.9	4592.9	4595.8	4597.4

4.3 Verification of the model

The correctness of the model has been evaluated by comparing it with values found in literature and experimental data. For a rod of 150 mm with a diameter of 25 mm, the ultrasonic wave of 1MHz was prescribed on the top of the rod. For the discretisation of the model, 8 element per wavelength were used with a Courant number of 1/10. The simulation is done for both copper and titanium.

4.3.1 Copper

The longitudinal wave speed of copper in literature is 4600 m/s. In a experimental study, using a copper buffer rod, Mastromarino verified this sound velocity [1]. The calculation of the longitudinal wave speed (c_l) can be done by combining equation 2.19 and 2.12 into:

$$c_l = \sqrt{\frac{E(1 - \nu)}{\rho(1 + \nu)(1 - 2\nu)}}, \quad (4.2)$$

where E is Young's modulus, ν is Poisson's ratio and ρ is the density of the solid. With the physical values of table 4.2, the calculated c_l becomes 4607 m/s. To verify the model, the wave speed is measured by calculating the difference in time between the initial wave and the reflected wave. This is measured at the top of the buffer rod, where the transducer is placed. Figure 4.4 shows the plot of the normalised stress measured at the top of the rod. The horizontal line, close to 0, represents the threshold. The script is written in a way that it detects when a smoother version of the stress measurements exceeds the threshold and it marks the point as the beginning of a peak.

Table 4.2: Physical and acoustic properties of the copper and titanium in the built-in library of COMSOL [25].

Material	Young's modulus (E)	Poisson's ratio (ν)	Density (ρ)
Copper	$1.2580 \cdot 10^{11}$	0.3350	$8.9377 \cdot 10^3 \text{ kg/m}^3$
Titanium	$1.0907 \cdot 10^{11}$	0.3386	$4.4995 \cdot 10^3 \text{ kg/m}^3$

The time travelled is measured as the time between the first and the second peak. This results in a longitudinal wave speed of 4597 m/s.

4.3.2 Titanium

For titanium, the value for the longitudinal wave speed as given by literature is 6070 m/s. The calculation of equation 4.2 with the properties of table 4.2 gives the longitudinal wave speed for titanium as 6091 m/s. Due to the lack of experimental data for a titanium buffer rod, another verification method is used. The software package called DISPERSE [20] gives the wave velocity of some ultrasonic wave in a solid. This gives 6060 m/s. Because only the demo-licence can be used, this verification method cannot be used for the simulation with copper. Figure 4.5 is a plot of the normalised stress at the top of the buffer rod. The speed of the wave is calculated as 6050 m/s. Since the values from the simulations in COMSOL are differing by less than 1% of the values of all other sources (see table 4.3), it can be concluded that the model is usable for the simulation of the buffer rod.

Table 4.3: Values of the longitudinal wave speed, to verify the ultrasonic model in COMSOL.

	literature	experimental	equation 4.2	Disperse	COMSOL sim.
Copper	4600	4600	4607.7	-	4597.4
Titanium	6070	-	6091.2	6060	6049.6

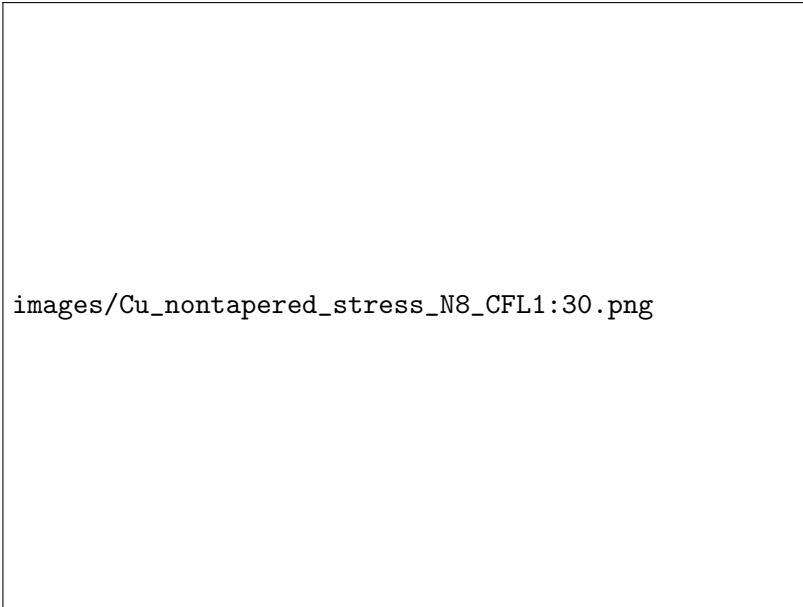


Figure 4.4: Pulse-echo response for non-tapered copper buffer rod for $N = 8$, $CFL = 1/10$, length of 150 mm, diameter of 25 mm and initial pulse of 1MHz.

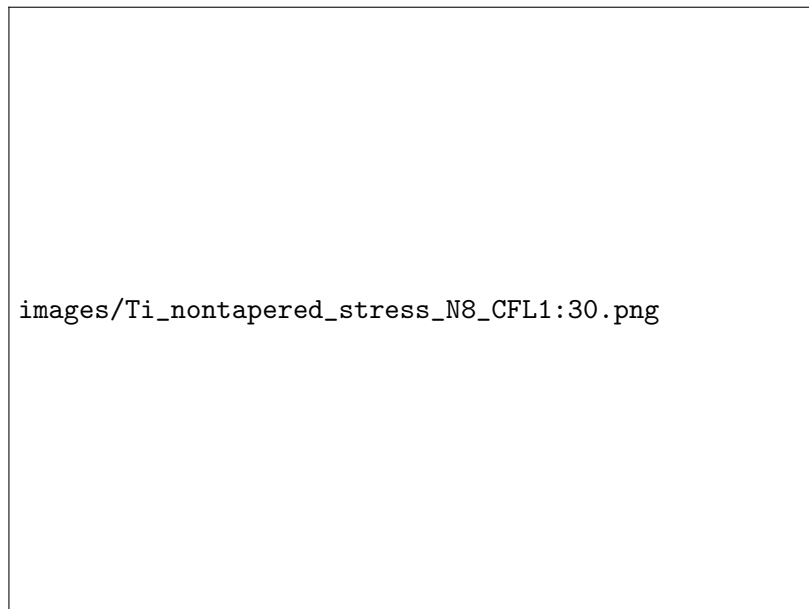


Figure 4.5: Pulse-echo response for non-tapered titanium buffer rod for $N = 8$, $CFL = 1/10$, length of 150 mm, diameter of 25 mm and initial pulse of 1MHz.

4.4 Tapering angle simulations

As explained in section 2.7.1, the goal is to reduce the trailing echo in the buffer rod. For the simulations, a double tapered buffer rod is used with angles of tapering (θ_t) between 1 and 2 degrees. It is also studied how the reduction of the trailing echoes changes when changing the diameter of the middle part of the buffer rod (l_d). For the simulations, the length of the buffer rod is 150 mm, 8 elements per wavelength are used and a CFL-number of 1/10 is used to define the time stepping. The reduction of the trailing echo is calculated by:

$$reduction = \frac{I_{t.e.}}{I_{f.p.}}, \quad (4.3)$$

where $I_{t.e.}$ represents the intensity of the first trailing echo and where $I_{f.p.}$ represents the intensity of the first reflected peak. These intensities are defined as the sum of the amplitude at the time points between the begin and the end of a peak. Table 4.4 gives, for buffer rods with different diameters, the optimal angle of tapering and the according trailing echo reduction (see appendix A for all data). It can be concluded that tapering the rod causes the trailing echoes to reduce. The table shows that the optimal tapering angle differs upon changing the diameter of the buffer rod. Whereas for a straight rod the head waves interfere constructively, this constructive behaviour is reduced when the rod is tapered. It can also be concluded that increasing l_d causes a decrease in the intensity of the trailing echo. Thus, the wider the buffer rod is, the better the SNR becomes.



Figure 4.6: Double tapered rod with length L , a diameter on the widest part of l_d and a tapering angle of θ_t

Table 4.4: Optimal angle of tapering for buffer rods with a diameter ranging from 20 to 40 mm. For the optimal angle, the reduction of the trailing echo is displayed.

diameter of buffer rod (l_d)	20 mm	25 mm	30 mm	35 mm	40 mm
optimal angle of tapering (θ_t)	1.7°	1.6°	1.5°	1.55°	1.65°
trailing echo reduction	0.513	0.439	0.326	0.237	0.184

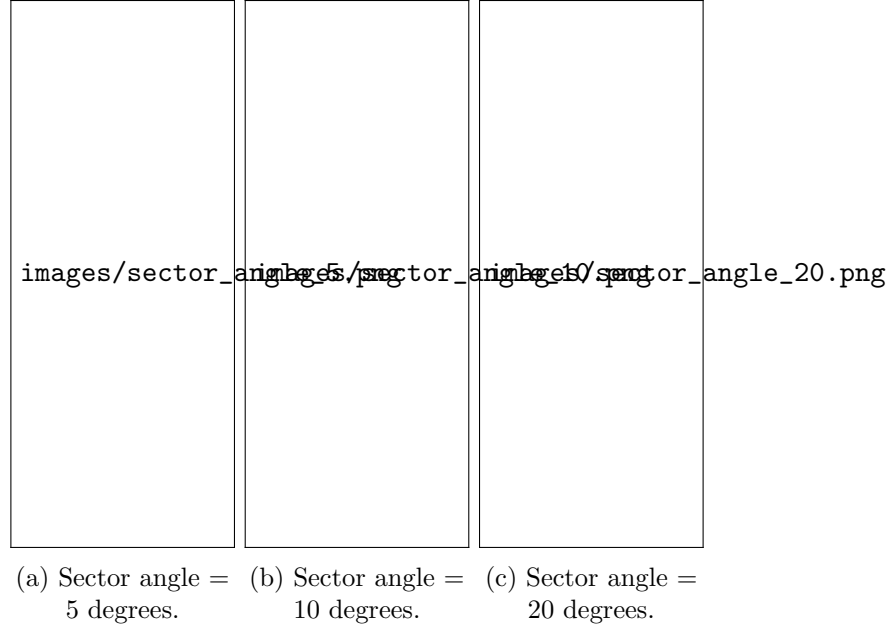


Figure 4.7: Mesh of the 3D model for different sector angles.

4.5 Reducing computation cost for 3D models

Simulations in 3D are more complex and heavy than in 2D, because more elements need to be calculated. In section 4.1, the minimum amount of elements for which the simulations are accurate enough is $N = 8$. When a 3D model of a buffer rod was simulated with a mesh density of eight elements per wavelength, the system on which the calculation was done failed. The simulation was too expensive and thus could not be run. This section aims at reducing the computation time for 3D models.

In order to reduce the computational cost of the model, the axial symmetry of the rod can be exploited. The simulation is calculated for only a sector of the rod. For the final plotting, this sector can be rotated around the radial axis of the rod. Some of the models are displayed in figure 4.7. Upon decreasing the angle of the sector, the total mesh elements decrease accordingly, resulting in a less expensive calculation. To check whether changing the sector angle has an impact on the accuracy of the simulation, multiple simulations are done by varying the angle. Since the simulations become too expensive when using $N = 8$, $N = 5$ will be used for these simulations. Also, in order to reduce the complexity of the mesh, the size of the buffer rod is reduced. The size of the simulated buffer rod is 40 mm long and 10 mm wide. Thus, it is important to note that the outcome is not physically representative for the simulation of the buffer rod. The only thing that is studied here is whether the idea of using the axial symmetry of the buffer rod can reduce the computational force required. The simulations are done for sector angles ranging between 2 and 20 degrees, using $N = 5$ and $CFL = 1/10$. The plots of the stress measured at the top of the rod are displayed in 4.8. What can be concluded from the plot is that decreasing the sector angle does not have a noticeable impact on the stress measurement. However, the computation time, seen in table 4.5, does decrease when decreasing the sector angle. It can be concluded that this simplification is useful in order to decrease the computation time of 3D models. Unfortunately, even when using a sector angle of 1, the model is still too complex to be calculated when $N = 8$ is used.

Table 4.5: Measurement of the computation time and the number of degrees of freedom for different sector angles.

sector angle	number of degrees of freedom	computation time
2 degrees	150876	17 minutes
5 degrees	168477	21 minutes
10 degrees	195072	23 minutes
20 degrees	381093	71 minutes



Figure 4.8: Stress at the top of the buffer rod versus sector angle in COMSOL Multiphysics, for a 3D buffer rod with a length of 40 mm and diameter of 10 mm. The prescribed displacement is a 1 MHz sinusoidal function with Gaussian window.

4.6 Comparison 2D and 3D models

The use of 2D axial symmetric models is desirable when simulating an ultrasonic waveguide through a cylindrical buffer rod. However, when using polygonal buffer rods, axial symmetric models can not be used. 3D models must then be used. This section aims at comparing 2D models with 3D models in COMSOL. As described in section 4.5, the 3D models could only be run for 5 elements per wavelength. The stress measurements for this comparison are therefore not physically correct, they only serve to investigate the difference between 2D and 3D models. For the comparison, all parameters must be the same for both models, except for the dimension. For both the 2D and 3D models, simulations are done for different buffer rods, one having a length of 40 mm and a diameter of 10 mm, the other having a length of 100 mm and a diameter of 25 mm. Figures 4.9a and 4.9b show the measurements at the top of the probes, for 2D and 3D simulations. From the plots, it can be concluded that the 2D model and the 3D model do not give the same results. The trailing echo comes in earlier for the 3D model then for the 2D model. A probable cause for the wave coming in earlier is dispersion and the creation of shear waves. In a dispersive medium, the speed of propagation of a wave is dependent on its frequency.



(a) Length = 40 mm, diameter = 10 mm

(b) Length = 100 mm, diameter = 40 mm

Figure 4.9: Plot of simulations for two buffer rods, where the stress at the top of the buffer rod is measured over time.

4.7 Polygonal buffer rods

Models have been made for the polygonal buffer rods to check the reduction of trailing echoes. The length of these models ranged from 50 mm to 100 mm. Unfortunately, because the buffer rods do not have as many symmetry planes as a circle, the models are too large to be computed. Also, for the simulation of irregular polygonal rods, the symmetry can not be used, since there is no symmetry. It could be concluded that stronger computer systems are required to study the behaviour of polygonal buffer rods.

Chapter 5

Conclusion

The goal for this research was to optimise a the simulation an ultrasonic wave propagating through a buffer rod. This optimisation was done to save computation time and increase the accuracy. Finally, the optimisation is also necessary to choose the best geometry for the rod and to give insight in what experimental set-up will be best to reduce trailing echoes. Reducing trailing echoes result in and increase of the signal-to-noise ratio. When the SNR increases, the attenuation of a wave inside the molten salt can be measured more accurately, thereby making the measurement of the viscosity more accurate.

For the discretisation of the model, the optimal amount of elements per wavelength (N) was found to be 8. The optimisation of the time-discretisation gave a CFL-number of 1/25. These parameters give an accurate result while also maintaining a reasonable computation time. The simulations could only be done for 2D axial symmetric models due to a lack of computation power to compute 3D models.

This research shows that the optimal angle of tapering differs for different diameters of the buffer rod. When using double tapered buffer rods, the trailing echoes decrease when increasing the rod's diameter. However, even after tapering the buffer rod, some trailing echoes are deteriorating the measurement of the attenuation. This is due to the fact that they are still measured at the same time as the signals emerging from the liquid. The idea of using polygonal buffer rods seemed promising, but, due to a lack of computational power it can not be numerically investigated.

5.1 Recommendation

When simulating an ultrasonic wave propagating through a buffer rod in COMSOL, the recommendation is to use a mesh with 8 elements per wavelength and to define the time step of the Time-Dependent Solver with a Courant number of 1/10. To increase computation time, the frequency can be reduced to 1MHz and the length of the rod for which the simulation is done can also be decreased.

Using irregular odd-n polygonal buffer rods can be seen as the potential solution to reduce trailing echoes. Also, the buffer rod could be cladded. This is the addition of a layer around the buffer rod with a specific acoustic impedance, the converted waves then will be transmitted into the cladding layer, instead of reflecting at the interface back into the rod.

The combination of cladding and using a tapered or polygonal buffer rod will increase the SNR, but still some trailing echoes will deteriorate the signal. Another technique, using surface waves, could potentially give better results. Elastic surface waves, such as Rayleigh or Love waves, can travel along the surface of a waveguide. When using surface waves, there is no deterioration of the measurement signal caused by mode conversion. This technique could greatly improve the SNR and could eventually result in accurate measurements of the viscosity and density of fluids at high temperature.

Appendices

Appendix A

Measurements for changing tapering angle

Table A.1: Reduction of the trailing echo for a buffer rod with a length of 150 mm and for different diameters.

angle	20 mm	25 mm	30 mm	35 mm	40 mm
1.0	1.471	0.796	0.510	0.399	0.278
1.1	1.297	0.716	0.452	0.364	0.258
1.2	1.109	0.629	0.400	0.324	0.238
1.3	0.965	0.559	0.369	0.288	0.218
1.4	0.816	0.503	0.338	0.260	0.201
1.45	-	-	0.328	-	-
1.5	0.694	0.470	0.326	0.240	0.190
1.55	-	-	0.328	0.237	0.188
1.6	0.585	0.452	0.337	0.238	0.187
1.65	-	-	-	0.244	0.184
1.7	0.535	0.453	0.371	0.253	0.184
1.75	0.513	-	-	-	-
1.8	0.513	0.449	0.405	0.274	0.187
1.85	0.517	-	-	-	-
1.9	0.535	0.448	0.439	0.301	0.219
2.0	0.553	0.439	0.474	0.328	0.227
2.1	-	0.435	-	-	-

Appendix B

Matlab code for wave speed determination

This Matlab script is used to post-process measurements of a parametric sweep in COMSOL. It calculated the wave speed by measuring the time of flight of the wave.

Listing B.1: Matlab code for wave speed calculation and measurement plotting

Bibliography

- [1] Mastromarino, S. (2016). *Determination of Thermodynamic properties of Molten Salt*, Ph.D. thesis, Delft University of Technology
- [2] World Nuclear Association, *Generation IV Nuclear Reactors*
- [3] SAMOFAR. Project - SAMOFAR. Retrieved from: <http://samofar.eu/project/>
- [4] H. Froeling. *Causes of spurious echoes by ultrasonic wave simulation*, BSc thesis, Delft University of Technology (2017).
- [5] J. Serp, M. Allibert, O. Beneš, S. Delpech, O. Feynberg, V. Ghetta, D. Heuer, D. Holcomb, V. Ignatiev, J.L. Kloosterman, L. Luzzi, E. Merle-Lucotte, J. Uhlíř, R. Yoshioka D. and Zhimin. The molten salt reactor (MSR) in generation IV: Overview and perspectives. *Progress in Nuclear Energy*, 77:308-319, 2014.
- [6] M. Allibert, D. Gérardin, D. Heuer, E. Huffer, A. Laureau, E. Merle, S. Beils, A. Cammi, B. Carlucci, S. Delpech, A. Gerber, E. Girardi, J. Krepel, D. Lathouwers, D. Lecarpentier, S. Lorenzi, L. Luzzi, S. Pומרouly, M. Ricotti, and V. Tiberi. Description of initial reference design and identification of safety aspects. Work Package 1, Deliverable D1.1, SAMOFAR (Safety Assessment of the MOlten Salt FAst Reactor. European project, Contract number: 661891, 2016.
- [7] T. Oud. Elastic wave simulation for buffer rod tapering. BSc thesis, Delft University of Technology, 2017.
- [8] T. Ihara, N. Tsuzuki, and H. Kikura. Development of the ultrasonic buffer rod for the molten glass measurement, *Progress in Nuclear Energy*, 82:176–183, 2014.
- [9] J. Pezant, J.E. Michaels and T.E. Michaels. An examination of trailing echoes in tapered rods. *AIP Conference Proceedings*, 1096:1627-1639, 2009.
- [10] F.B.M. Foudzi, Development of Polygonal Buffer Rods for Ultrasonic Pulse-Echo Measurements with High Signal-to-Noise Ratio. Ph.D. thesis, Nagaoka University of Technology, 2014.
- [11] V.S.K. Prasad, K. Balasubramaniama, E. Kannan and K.L. Geisinger, Viscosity measurements of melts at high temperatures using ultrasonic guided waves, *Journal of Materials Processing Technology* 207(1):315-320, 2008.
- [12] Hisham, Comsol convergence tips. Retrieved from: <https://community.cmc.ca/docs/DOC-1453>, 2012.

- [13] B. Ghose, K. Balasubramaniam, C.V. Krishnamurthy and A.S. Rao, *Two dimensional fem simulation of ultrasonic wave propagation in isotropic solid media using comsol*, COMSOL Conference, 2010.
- [14] J.David, N. Cheeke, *Fundamentals and applications of ultrasonic waves*, CRC Press LLC, 2002.
- [15] S. Delpech, E. Merle-Lucotte, D. Heuer, M. Allibert, V. Ghetta, C. Le-Brun, X. Doligez and G. Picard. Reactor physic and reprocessing scheme for innovative molten salt reactor system. *Journal of Fluorine Chemistry*, 2008.
- [16] E. Capelli. Thermodynamic characterization of salt components for molten salt reactor fuel. Ph.D thesis, Delft University of Technology, 2016.
- [17] R.S. Moore and H.J McSkimin. Dynamic shear properties of solvents and polysterene solutions from 20 to 300 MHz. *Physical Acoustics*, 6:167-242, 1970.
- [18] W.P. Mason, W.O. Baker, H.J McSkimin and J.H. Heiss. Measurement of shear elasticity and viscosity of liquids at ultrasonic frequencies. *Physical Review*, 75(6): 936-946, 1949.
- [19] Reflection and transmission of ultrasonic waves. Retrieved from: <http://www.fast.u-psud.fr/~martin/acoustique/support>, n.d.
- [20] M. Lowe, Disperse - Guided wave dispersion curve calculation, Imperial College NDT lab, n.d.
- [21] *Comparison of lifecycle greenhouse gas emission of various electricity generation sources*, WNA report, retrieved from: <http://www.world-nuclear.org/>, 2011.
- [22] S. Mönkölä, Numerical simulation of fluid-structure interaction between acoustic and elastic waves, *Jyväskylä studies in computing*, 133:1456-5390, 2011.
- [23] Snells law2.svg. Wikimedia Commons, the free media repository. Retrieved from https://commons.wikimedia.org/w/index.php?title=File:Snells_law2.svg&oldid=260114417.
- [24] H. Sönnerlind, Why All These Stresses and Strains?, retrieved from: <https://www.comsol.com/blogs/why-all-these-stresses-and-strains/>, 2013.
- [25] COMSOL Multiphysics® v. 5.2a. COMSOL AB, Stockholm, Sweden, 2015.
- [26] MATLAB Release 2016a, The MathWorks, Inc., 2016.